Master's thesis

Ingeborg Monge Christoffersen

A numerical study of turbulent mixing in coaxial jets

Trondheim June 2010

NTNU
Norwegian University of Science and Technology
Faculty of Natural Science and Technology
Department of Physics

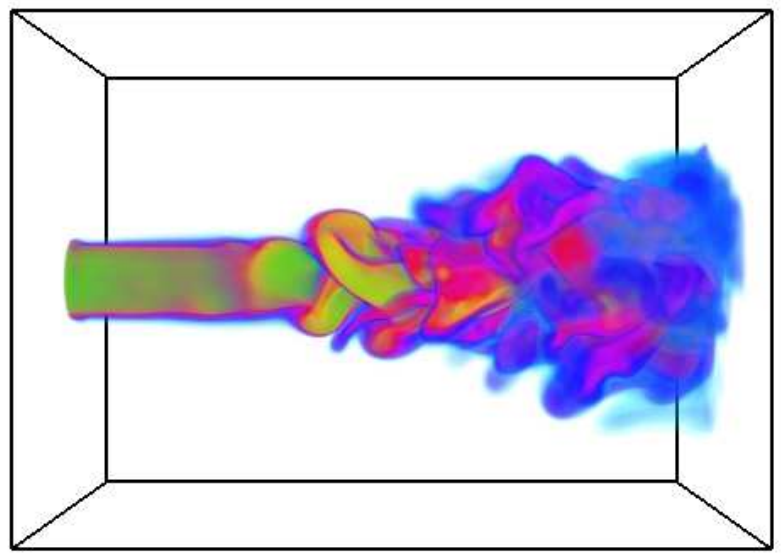

NTNU
Norwegian University of
Science and Technology

NTNU
Norwegian University of
Science and Technology

Ingeborg Monge Christoffersen

A numerical study of turbulent mixing in coaxial jets

Master's thesis

Trondheim, June 2010

Norwegian University of Science and Technology
Faculty of Natural Science and Technology
Department of Physics

Academic supervisor: Nils Erland L. Haugen

NTNU
Norwegian University of
Science and Technology

Abstract

Direct numerical simulations (DNS) of round and coaxial jets are performed. The Pencil Code is used for generating the three-dimensional and time-dependent flow field. Mixing is investigated by implementation of a passive scalar in the simulations.

The primary objective of the work is to study mixing properties of the passive scalar in the coaxial jets. Three simulations with different outer to inner jet exit velocity ratios are therefore conducted for comparison. The results for the time-averaged mean velocities and the mean passive scalar fields are presented together with their associated turbulence fluctuations. Mixing is contemplated according to these results, the potential core lengths and the downstream locations of where self-similarity is obtained. The results show reasonable agreement with existing literature.

The studies of the round jets aim to validate the use of the Pencil Code on simulations of turbulent jets.

Preface

Background

This report is written as the master thesis required to obtain the degree Master of Science in Applied Physics at the Norwegian University of Science and Technology (NTNU). The work was carried out during the 10th semester of the degree and it covers 30 credit units (studiepoeng). This corresponds to approximately 900 hours over 20 weeks. The workload includes acquiring completing knowledge through literature studies, setting up project goals and implementing suggested solutions in addition to writing this final report. This report documents the work done and the results obtained.

The thesis work was carried out at SINTEF Energy Research under the supervision of Nils Erland L. Haugen. SINTEF is Scandinavia's largest independent research organization and is an important collaborator to many companies in Norway and abroad. Also, SINTEF has a close collaboration with NTNU.

Acknowledgments

I would like to thank my external supervisor Nils Erland L. Haugen at SINTEF Energy Research. I have worked closely with Haugen during this semester, and he has always been available and open to my ideas and questions. I would also like to thank Jon Andreas Støvneng at the Department of Physics at the Norwegian University of Science and Technology for being my formal supervisor.

In addition, I would like to express gratitude to Solveig Søvik Alnes and Anders Granskogen Bjørnstad for inspirational and helpful discussions. They have also been writing their thesis for SINTEF this semester, using the Pencil Code. In closing I would like to thank Halvor Lund for critical reading of this report.

Contents

List of Figures

List of Tables

Chapter 1

Introduction

Round jets are commonly studied both experimentally and numerically because of their easy configuration. A round jet can be defined as the flow one gets when a naturally evolving fluid is issued from a circular orifice. The main purpose of this project was to investigate turbulent mixing processes in a coaxial jet. A coaxial jet forms when the fluid is issued from a central and a co-annular orifice. Coaxial jets are considered as an effective method for mixing of two different fluids. The coaxial jet configuration is widely used in industrial application for effective mixing, e.g. in combustion devices. The motivation for the present work was for application in hydrogen double gas turbines. It is crucial for the hydrogen to mix properly with the warm exhaust in the second combustion chamber to prevent explosion.

Before one can start to investigate the mixing processes in a coaxial jet, it is necessary to acquire some basic knowledge of turbulent flows and the jet configurations. Chapter 3 and chapter 4 presents the necessary theory of the subject.

In the first part of the 19th century the Irish mathematician George S. Stokes and the French engineer Claude Navier independently found that all fluid flows are governed by a partial differential equation later named the Navier-Stokes equations (White, 2005). The Navier-Stoke equations express the conservation of momentum for a flow. The equations are seemingly quite simple, but it has solutions that are not fully understood even to this day.

The behavior of a fluid flow is very dependent on the viscosity of the fluid. Towards the end of the 19th century, Osborne Reynolds did a number of experiments where he studied the transition between laminar and turbulent flows. A dimensionless parameter which correlates to the viscous behavior of fluids was later named after him (White, 2005). The Reynolds number is the ratio of inertial forces to the viscous forces in the flow. A low Reynolds number indicates a viscous, smoothly varying, laminar flow, whereas a high Reynolds number implies a turbulent flow with fast varying velocity fluctuations.

A turbulent flow consists of a large range of scales, both length scales and time

scales. In the 1940s, Andrey Kolmogorov introduced his ideas of the smallest scales in a turbulent flow. In his *universal equilibrium theory* he argues that the smallest scales in a flow are statistically independent of the large scale, i.e. the large-scale turbulence and the mean flow. The smallest scales are similar for every turbulent flow (Tennekes and Lumley, 1983). Kolmogorov found that the smallest length scale, velocity scale, and time scale were all functions of the energy dissipation rate and the viscosity. The dissipation is the process where energy is converted into heat and is due to the viscous forces in the flow. The viscous forces destroy the smallest eddies and convert their energy into thermal energy.

Turbulent flows are still considered one of the last unsolved problems in classical physics. The state of turbulence is unsteady, three-dimensional and extremely complex. However, all the characteristics of turbulent flows are embodied in the Navier-Stokes equations for fluid motions. For turbulent flows the solutions to these equations are complex and must be found numerically. This has only been possible since the 1980s after the many advances in computer science. Directly solving the Navier-Stokes equations with numerical methods is called direct numerical simulations (DNS) and today the data produced by DNS is considered as valid as data from experiments. DNS use no models or approximations to solve the Navier-Stokes equations, i.e. the whole range of spatial and temporal scales in the turbulence is resolved. This puts requirements on the computational mesh which results in calculations demanding many CPU hours. In engineering it is therefore usual to make use of turbulence models to keep the computational costs at a minimum. These computational methods are Reynolds-averaged Navier-Stokes (RANS) and large eddy simulation (LES). The numerical methods are further discussed in chapter 2.

Several work on turbulent jets, both numerical and experimental are published. To mention some, experimental studies of a round jet were done by Panchpakesan and Lumley (1993) and Hussein et al. (1994). Lubbers et al. (2001) did one of the first numerical investigations of mixing of a passive scalar in a round jet. In 1992 Dahm et al. (1992) published a work on both experimental and numerical investigations of the near field of a coaxial jets. In Rehab et al. (1997) and Villermaux and Rehab (2000), there were done experiments on mixing and investigation of the flow regimes in coaxial jets with water. Warda et al. (1999) also did experimental studies of coaxial jets, where they focused on the effect of different outer to inner jet velocity ratios. More recent numerical investigations on coaxial jets have been done by Silva et al. (2003), Balarac and Si-Ameur (2005) and Dinesh et al. (2010).

Chapter 2

Numerical methods

The fundamental equations of fluid flows are seemingly simple, but most of the solutions are so complex that they must be obtained numerically. All the simulations presented in this work were performed with the Pencil Code.

2.1 Fluid equations

The Navier-Stokes equations describe the motion of a fluid. The equations are mainly derived from the fact that momentum is conserved. Generally the Navier-Stokes equations for a compressible fluid read

$$\frac{\partial \mathbf{U}}{\partial t} + \mathbf{U} \cdot \nabla \mathbf{U} = -\frac{1}{\rho} \nabla P + \frac{1}{\rho} \nabla \cdot (2\nu\rho\mathbf{S}) + \frac{\mathbf{F}}{\rho} \tag{2.1}$$

$$\frac{\partial \rho}{\partial t} + \nabla \cdot (\rho \mathbf{U}) = 0, \tag{2.2}$$

where $\mathbf{U}$ is the fluid velocity vector, ρ is the density of the fluid, P is the pressure, ν is the kinematic viscosity of the fluid, $\mathbf{S}$ is the traceless rate of strain tensor, and $\mathbf{F}$ is the sum of all other body forces per volume acting on the fluid, e.g. gravity. The traceless rate of strain tensor,

$$S_{ij} = \frac{1}{2} \left(\frac{\partial u_i}{\partial x_j} + \frac{\partial u_j}{\partial x_i} \right) - \frac{1}{3} \delta_{ij} \frac{\partial u_k}{\partial x_k}, \tag{2.3}$$

describes how fast the velocity components change in each of the three directions.

Equation 2.1 is referred to as the momentum equation. The left hand side of this equation is related to the inertia of the fluid. The first term on the left hand side can be recognized as the local acceleration, while the second term is the convective acceleration, i.e. the time independent acceleration of the fluid (White,

2005). On the right hand side of the momentum equation the forces are represented. The right hand side consists of the pressure force, the viscous forces, and the body forces. Equation 2.2 is referred to as the mass continuity equation.

No general solution of the Navier-Stokes equations is known. Actually, the Navier-Stokes equations only have analytical solutions to the simplest laminar cases, thus one has to rely on numerical methods to obtain solutions for realistic cases. However, the solutions of the Navier-Stokes equations are very complex and it is not even proven that all solutions exists. This is why fluid turbulence is sometimes referred to as one of the major unresolved problems in classical physics.

In statistical studies of the equation of motion one ends up with more unknowns than equations. This is called the closure problem of turbulence theory. Thus, it is necessary to make assumptions about the flow to obtain solutions. It is usual to make use of a simple equation of state, i.e. a connection between the pressure and the density of a flow.

2.2 Computational fluid dynamics

Numerical methods are widely used both in engineering and in research to solve the Navier-Stokes equations for flow motion. Such models are for example Reynolds-averaged Navier-Stokes equation (RANS), Large eddy simulations (LES), and Direct numerical simulations (DNS).

In engineering it is often good enough to use a turbulence model to solve the equations for some mean quantities. This is easier and faster than to solve the Navier-Stokes equations directly, and most importantly it will keep the numerical costs at a minimum. RANS and LES make use of such models.

RANS is the standard numerical method for simulating flow motion for the industry today. The idea of RANS is to decompose the velocity vector into a mean part and a fluctuating part and averaging the Navier-Stokes equations in time, making the solutions time independent. The obtained RANS equations governs the mean flow. It is found that the only parts of the turbulence that influence the mean flow are some random turbulent fluctuations, called the Reynolds stresses, $\overline{u_i u_j}$. Thus, it is only necessary to model the Reynolds stresses to simulate the turbulent flow.

RANS gives good results for simple flows, but may not be reliable in all cases. In computational turbulence research it is important to simulate the turbulent flow without any models, i.e. one has to resolve all the scales of the flow to obtain accurate results. This type of simulation is called DNS.

Since DNS needs to resolve all the scales in the flow, both spatially and temporally, the computational mesh size has to be comparable to the smallest length scale of the flow and the time step must be comparable to the inverse of the highest

frequencies. This requires a lot of memory and many CPU hours, and in addition huge amounts of data is produced.

In contrast to laboratory study, one can deduce the correlations between the fluctuating quantities and obtain extremely detailed information of the flow structures with DNS. In addition, many experiments which are too difficult or expensive in the laboratory can be implemented with DNS. However, there are some limitations regarding DNS. The most important one is that DNS is limited to fairly low Reynolds numbers due to cost considerations. Another important limitation of DNS is the issue of specifying open boundary conditions. The difficulties for inflow and outflow boundary conditions get even worse for compressible fluids (Moin and Mahesh, 1998).

In LES, the fluid motions for the largest scales are represented directly as in DNS, while the smaller scales are modeled. This makes the computational costs of LES somewhere in between RANS and DNS.

The present work uses DNS because it was found necessary to make sure that all scales are resolved. In the future, it could be convenient to use LES to keep the computational cost lower and to be able to do simulations with higher Reynolds numbers. It would then be important to use the DNS results to validate the modeling of the LES.

2.3 The Pencil Code

All the simulations presented in this work were performed with the Pencil Code. The Pencil Code is a higher order finite difference code originally designed to deal with weakly compressible turbulent flows (Pencil Code Manual). The code is written in Fortran 90 and is used to solve the Navier-Stokes equations and other types of partial differential equations. The methods used are 3rd order explicit Runge-Kutta in time and 6th order central spatial discretization. The coordinate system is Cartesian.

The spatial discretization must be of high order to resolve all the scales in the flow and give realistic results for an affordable resolution. As pointed out in Moin and Mahesh (1998), Fourier spectral schemes are more accurate and give smaller resolution requirements. The Pencil Code uses a central difference scheme because it is faster and it makes implementation of non-periodic boundaries and parallelization easier. The 6th order spatial derivatives give the accuracy needed. The code uses MPI (Message Passing Interface) for communication between processors on multiprocessor computers. The processors divide the domain so that they solve for an equal amount of grid points. Around each of these sub-domains there is a layer consisting of three mesh-points, called “ghost zones”, for the derivations.

The Pencil Code is based on an explicit formalism rather than an implicit

formalism which is more computationally demanding. Explicit formalisms use the current state of the system to find the solution of the system at the next time step.

Chapter 3

Turbulence

Most fluid flows are turbulent, and can be found many places on an everyday basis. This chapter presents some characteristics of turbulent flow to give a broader understanding of the nature of turbulence.

3.1 Turbulent flows

Turbulent flows can be characterized by four attributes. The flows are irregular, turbulent diffusive, three-dimensional and they have a large Reynolds number (Tennekes and Lumley, 1983).

Figure 3.1 gives a picture of the differences between a laminar and a turbulent flow. In the laminar region the velocity field vectors are all parallel, but as soon as the flow becomes turbulent, velocity fluctuations, denoted u' and v' in figure 3.1, of all sizes appear in the flow. The velocity fluctuations make the flow irregular, chaotic and random. In spite of the chaos and randomness, the flow is a solution of the Navier-Stokes equations.

In a turbulent flow the turbulence is diffused. In all flows, heat, mass, and momentum are transported from areas with high concentration to areas with lower concentration. The special feature with a turbulent flow is that also turbulence is diffused. By saying that turbulence is diffused, it is meant that there is a spreading of velocity fluctuations. This increases the diffusion of mass, heat, and momentum with many orders of magnitude compared to molecular diffusion, resulting in a more rapid mixing. This is visualized in figure 3.1 where a dye is put into the flow and it is seen that it is not mixing in the laminar region, but in the turbulent region it is rapidly mixed in the flow.

In addition to velocity fluctuations, high level vorticity fluctuations play an important role in turbulent flows. The vorticity $\boldsymbol{\omega}$ is the curl of the velocity vector,

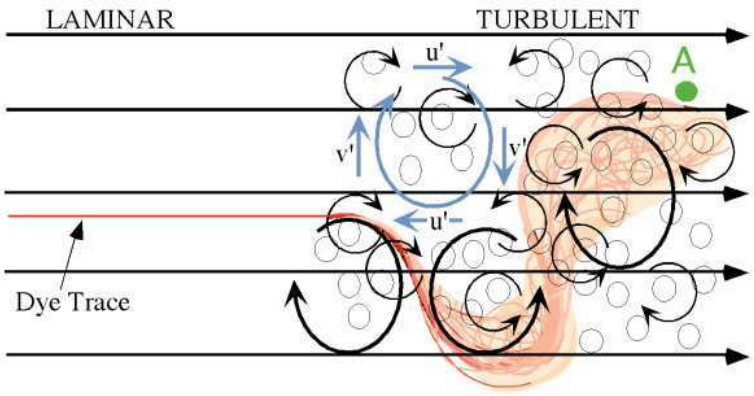

Figure 3.1: Transition between laminar and turbulent flow (MIT Open Courseware).

$$\boldsymbol{\omega} = \nabla \times \mathbf{U}. \tag{3.1}$$

Vortex stretching is essential in production of turbulence and is an important mechanism to maintain vorticity. The curl of the Navier-Stokes equations describes the evolution of vorticity. The left hand side of the equations becomes

$$\begin{aligned}
&\nabla \times \left(\frac{\partial \mathbf{U}}{\partial t} + \mathbf{U} \cdot \nabla \mathbf{U} \right) = \\
&\frac{\partial (\nabla \times \mathbf{U})}{\partial t} + \mathbf{U} \cdot \nabla (\nabla \times \mathbf{U}) - (\nabla \times \mathbf{U}) \cdot \nabla \mathbf{U} + (\nabla \cdot \mathbf{U}) (\nabla \times \mathbf{U}) = \\
&\frac{\partial \boldsymbol{\omega}}{\partial t} + \mathbf{U} \cdot \nabla \boldsymbol{\omega} - \boldsymbol{\omega} \cdot \nabla \mathbf{U},
\end{aligned} \tag{3.2}$$

where $\nabla \cdot \mathbf{U} = 0$ is used for convenience (incompressible flow). The last term, $\boldsymbol{\omega} \cdot \nabla \mathbf{U}$, is referred to as the vortex stretching term (Pope, 2000). The x-component of this term,

$$\left(\frac{\partial w}{\partial y} - \frac{\partial v}{\partial z} \right) \frac{\partial u}{\partial x} + \left(\frac{\partial u}{\partial z} - \frac{\partial w}{\partial x} \right) \frac{\partial u}{\partial y} + \left(\frac{\partial v}{\partial x} - \frac{\partial u}{\partial y} \right) \frac{\partial u}{\partial z}, \tag{3.3}$$

is, like the two other components, dependent on three dimensions. In other words, the vorticity fluctuations will not be produced if the velocity fluctuations only exist in two dimensions. This is why a turbulent flow has to be considered in all three spatial dimensions. Turbulence cannot maintain itself, it needs energy supply, e.g.

the shear in the mean flow. It is the interactions between vorticity vectors and velocity gradients that create and maintain the turbulence in a flow.

A flow is either turbulent, laminar or in a transition state in between depending on the Reynolds number of the flow. The Reynolds number is defined as

$$\mathrm{Re} = \frac{UL}{\nu}, \tag{3.4}$$

where U and L are the characteristic velocity and length scales of the flow, and ν is the kinematic viscosity. For instance, in the case of a jet, the characteristic velocity can be the jet velocity, and the characteristic length can be the jet's diameter. Viscosity is a measure of the fluid's resistance to flow. Air has low viscosity, while e.g. syrup has high viscosity. Kinematic viscosity is defined as $\nu = \mu/\rho$, where μ is viscosity and ρ is the density of the fluid. A flow becomes turbulent when the Reynolds number is sufficiently high. High Reynolds number indicates instability in viscosity versus inertia in the flow, which results in turbulence.

3.2 Turbulent scales

Eddies of many different sizes are formed due to the turbulence in a flow. The largest eddies get their energy from the mean flow and have a length scale on the order of magnitude as the width of the flow. The nonlinear terms in the equation of motion create smaller and smaller eddies until the smallest eddies are destroyed by the viscosity of the fluid. Thus, the viscosity determines the dimensions of the smallest scales in the flow. The kinetic energy of the smallest eddies is dissipated into thermal energy. The process where smaller and smaller eddies are created is called the turbulence cascade process. The largest eddies transport most of the momentum, heat and mass and contain most of the energy whereas the smallest eddies contain little energy but have higher vorticity than the larger scales.

The largest scales in the flow are L, U and t for length, velocity and time, respectively. The scales of the smallest eddies in the flow are called the Kolmogorov microscales. Kolmogorov argued that the small time scale of the smallest eddies made them statistically independent of the relative slow large scale turbulence and of the mean flow. Thus, as Kolmogorov concluded in his *universal equilibrium theory*, the small scales will be similar in all turbulent flows (Tennekes and Lumley, 1983). The small scales do not remember the structure or orientation of the large scales which indicates that the small scales are close to isotropic, i.e. independent of direction.

The Kolmogorov microscales for length, velocity and time are defined as (Tennekes and Lumley, 1983),

$$\eta \sim \left(\frac{\nu^3}{\epsilon}\right)^{1/4}, \quad v \sim (\nu\epsilon)^{1/4} \quad \text{and} \quad \tau \sim \left(\frac{\nu}{\epsilon}\right)^{1/2}, \tag{3.5}$$

where ν is the kinematic viscosity and ϵ is the energy dissipation rate. It can be assumed that the dissipation rate is on the order of the energy supply rate from the larger scales to the smaller scales. Thus, the dissipation rate can be connected to the largest scales by

$$\epsilon \sim U^2 \cdot t = U^2 \cdot \frac{U}{L} = \frac{U^3}{L} \tag{3.6}$$

This gives the relation between small scales and large scales,

$$\frac{\eta}{L} \sim \left(\frac{UL}{\nu}\right)^{-3/4} = \mathrm{Re}^{-3/4}. \tag{3.7}$$

The relation is directly dependent on the Reynolds number, resulting in an increasing range of scales with an increasing Reynolds number. This is the reason why DNS simulations are limited to relatively low Reynolds numbers. In addition, a smaller time step is required for higher Reynolds number following

$$\tau \sim \frac{\eta}{v} \sim \frac{L}{U}\left(\frac{\nu}{UL}\right)^{1/2} = \frac{L}{U}\mathrm{Re}^{-1/2}. \tag{3.8}$$

Thus, a higher Reynolds number requires a finer grid and a smaller time step, which demands more memory and CPU hours.

Even though there is a wide range of scales in turbulent flows, the smallest scales are much larger than the molecular length scales. Thus, a turbulent flow can be treated like a continuum. This is important to note since the Navier-Stokes equations are valid only for continuums.

Chapter 4

Turbulent jets

In this chapter an introduction to the basic concepts of jets is given. The material is mainly found in chapter 5 in Pope (2000).

4.1 The round jet

A round jet appears when a fluid is fed through an axisymmetric source with a higher velocity than the surroundings, and it is spread free from external forces. Because of its easy configuration, jets are one of the most studied turbulent free shear flows. A turbulent free shear flow is characterized by a mean velocity gradient that develop in the absence of solid boundaries. The turbulence is generated by the mean velocity shear.

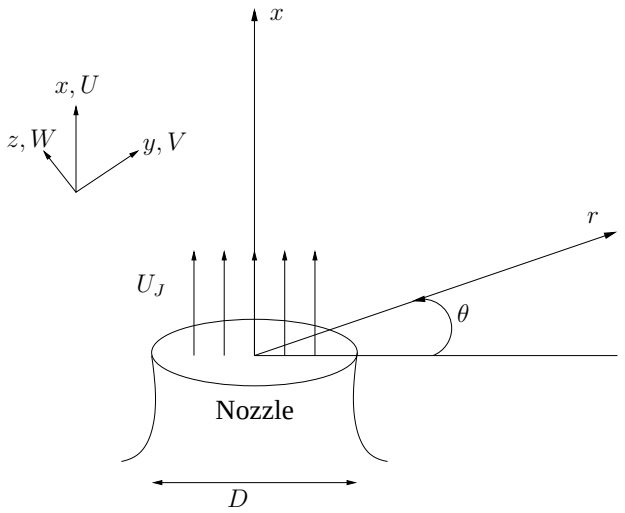

Figure 4.1: A sketch of the configuration in round jet experiments.

Figure 4.1 shows the configuration and coordinate system for a round jet. The nozzle ideally produces an approximately flat topped velocity profile, with velocity U_J. The jet flows into a fluid that initially is at rest or has a low coflowing velocity. The flow is statistically stationary and axisymmetric. The velocity components in the x, y, and z directions are denoted U, V, and W. The Reynolds number for a round jet is defined by $\mathrm{Re} = U_J D/\nu$, where U_J is the jet exit velocity, D is the nozzle diameter, and ν is the kinematic viscosity of the fluid. The Reynolds number can be considered the most important parameter for the round jet. When the Reynolds number is sufficiently high, turbulent structures will form in the shear layer. Figure 4.2 shows a picture of a round jet. It is seen that the jet spreads out in the radial direction. This implies that the velocity in the x direction decreases.

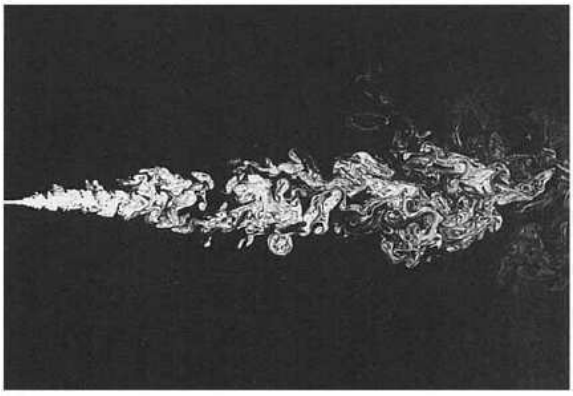

Figure 4.2: Photograph of the concentration in a round jet with Re=1500 (Dahm and Dimotakis (1990)).

When the evolution of jets is studied, one is often interested in how the jet spreads and how the centerline velocity behaves. The centerline velocity is denoted U_0. The velocity in the coflow is denoted U_a. In figure 4.3 a schematic diagram of the jet evolution is given. The flow consists of three different regions, the potential core, the mixing layer, and the surrounding region. The potential core is an irrotational region where $U = U_J$ and where there are no spanwise or normal velocities. The streamwise location where the potential core ends is denoted $x = x_c$. The region where the potential core is still present is called the zone of flow establishment. After the two mixing layers merge at the end of the potential core, the zone of established flow begins. Somewhat downstream of x_c the flow becomes a fully developed turbulent flow.

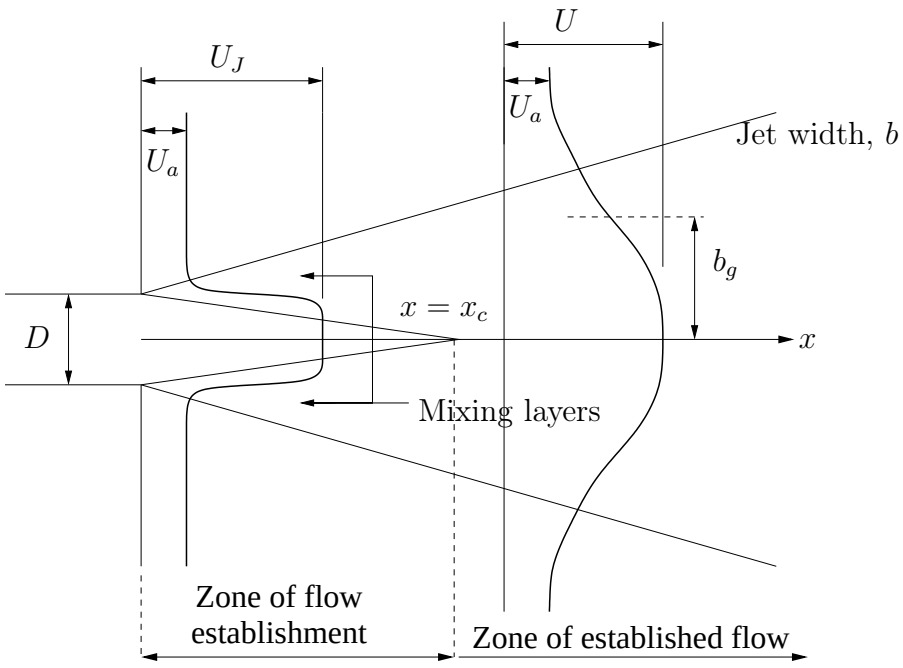

Figure 4.3: Schematic diagram of round jet in coflow

4.2 Mean properties and self-similarity

A turbulent flow is always time-dependent, but on average it can be steady. Thus, it is necessary to consider average properties to describe it. The instantaneous quantity is decomposed into the mean value and a fluctuating part. For instance for the velocity field one gets

$$U_i = \langle U_i \rangle + u_i', \tag{4.1}$$

where $\langle U_i \rangle$ is the mean velocity and u_i' is the fluctuating velocity in the x_i-direction. The velocity profiles shown in figure 4.3 represents the mean velocity. The shape of the profile in the zone of established flow is Gaussian, and a special feature of jet flows is that this shape does not change after the fully developed region. The velocity profile of $\langle U \rangle / U_o$ becomes self-similar.

The concept of self-similarity is important in studies of turbulent flows. The idea is that if you have a quantity $Q(x, y)$ that depends on two independent variables, and it can be scaled in such a manner that it keeps the same shape it is self-similar. That is, if there exists characteristic scales $Q_0(x)$ and $\delta_0(x)$ for $Q(x, y)$ such that

$$\xi \equiv \frac{y}{\delta_0(x)} \tag{4.2}$$

$$\tilde{Q}(\xi, x) = \frac{Q(x, y)}{Q_0(x)}, \tag{4.3}$$

are independent of x, then there will be a function $\hat{Q}(\xi)$ such that $\tilde{Q}(\xi, x) = \hat{Q}(\xi)$ and $Q(x, y)$ is self-similar, only dependent on one independent variable, $Q_0(x)$, $\delta_0(x)$, and $\hat{Q}(\xi)$ (Pope, 2000).

For a round jet typical similarity coordinates for the cross stream are $r/r_{1/2}$, $r/(x - x_0)$ or r/b_g, where $r_{1/2}$ is found where $\langle U(x, r_{1/2})\rangle = \frac{1}{2}U_0(x)$ and x_0 is the virtual origin of the jet. In the present work r/b_g is used. The velocity half-width, b_g, is defined by the radial location at which $\langle U(x, b_g)\rangle = e^{-1}U_o(x)$. For a round jet in a stagnant environment it is found that,

$$\frac{U_0(x)}{U_J} \sim \frac{1}{x - x_0}, \tag{4.4}$$

$$b_g \sim x \tag{4.5}$$

$$\frac{\langle U\rangle}{U_0} = \exp\left(-\frac{r^2}{b_g^2}\right). \tag{4.6}$$

If the coflow is very small, it can be assumed that it does not influence the jet dynamics very much.

4.3 The coaxial jet

A coaxial jet is a jet that appears when there is a co-annular source in addition to the central source and the fluids are fed in at different velocities through the sources. The coordinate system is the same as for the round, single jet. The coaxial jet configuration is known as a simple way to mix two fluids. It is also a convenient configuration for instance for cooling the inner jet.

Figure 4.4 shows a schematic diagram of the downstream evolution for a coaxial jet. In this case there will be two potential cores and four mixing layers. The location of the end of the potential cores are here denoted $x_{c,1}$ for the inner one, and $x_{c,2}$ for the outer. It can be argued that the length of the potential cores depends on the outer to inner velocity ratio, r_u, and the ratio of outer to inner diameters of the coaxial jet, β, defined as

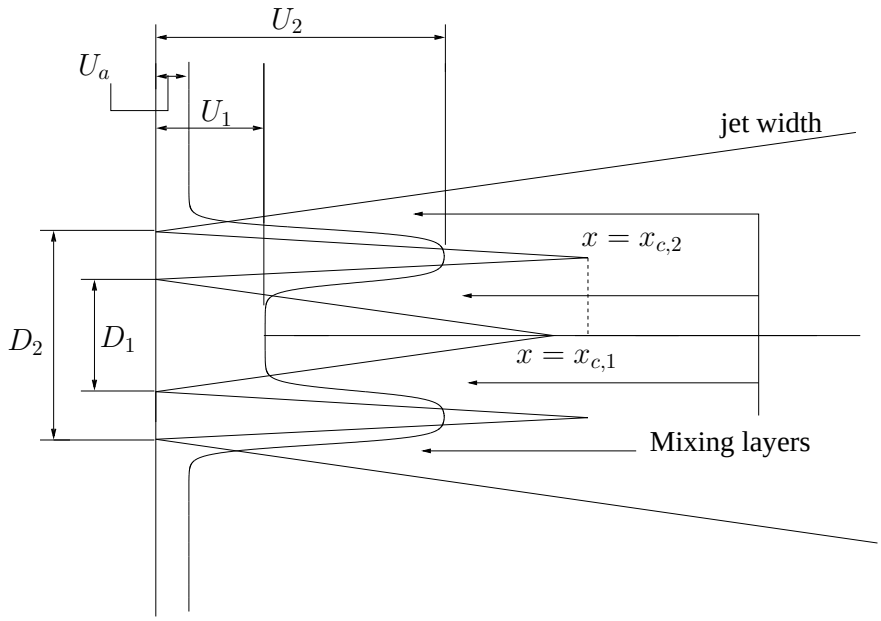

Figure 4.4: Schematic diagram of coaxial jet with a coflow

$$r_u = \frac{U_2}{U_1} \tag{4.7}$$

$$\beta = \frac{D_2}{D_1}, \tag{4.8}$$

where U_2 is the velocity of the co-annular flow, U_1 is the velocity of the inner jet, D_2 and D_1 is the diameters of the outer and inner jet, respectively. The velocity of the coflow is denoted U_a also for the case of coaxial jets.

Chapter 5

Entrainment models in coflowing environments

Entrainment is the incorporation of the fluid from the surroundings into the jet (Enjalbert et al., 2009). The turbulent eddies generated in the shear layer between the jet and the surroundings mix fluid from the surroundings into the jet. An inflowing entrainment velocity, u_e, can be introduced as the velocity at jet width, b (see figure 4.3). The entrainment models considered here are those presented in Chu et al. (1999), Lee et al. (2003), and Rehab et al. (1997).

The entrainment models deal mainly with the self-similar region of the jets. The scope of these considerations will be to find out if it is possible to use these models for finding a prediction of the length of the potential cores, both for the single jet and the coaxial jet.

5.1 Prediction of potential core length for a single jet

As discussed in the previous chapter, it is found that $U_0(x)$ decays as x^{-1} and that the jet spreads linearly, $b_g \sim x$, for a jet in a stagnant environment. For a single jet in coflow, the case is a little different. In Chu et al. (1999) there is given a derivation of the spreading rate for a single jet in coflow. They use a top-hat velocity profile as the characteristic velocity profile to obtain the results. The derivations are done by momentum conservation considerations. The idea of the top-hat velocity profile is that the mass and momentum flux integrals will be easier to evaluate. The expression Chu et al. (1999) end up with for the spreading rate is

$$\frac{\mathrm{d}b_g}{\mathrm{d}x} = \frac{\beta_s}{\sqrt{2}} \frac{U_0 - U_a}{U_0 + U_a}, \tag{5.1}$$

where $\beta_s = 0.154$ is a constant derived from the spreading rate of single jet in stagnant ambient.

Now the top-hat approach uses $b_g = B/\sqrt{2}$, where B equals the width of the top hat profile. Knowing that at the inlet $B = D$, and at the end of the potential core B equals the jet width, one finds

$$\frac{B}{D} = \frac{1}{\sqrt{1 + U_a/U_J}}. \tag{5.2}$$

The centerline velocity inside the potential core equals the jet exit velocity, so the combination of equation 5.1 and 5.2 gives,

$$\frac{x_c}{D} = \frac{\sqrt{1 + U_a/U_J}}{\beta_s(1 - U_a/U_J)}. \tag{5.3}$$

5.2 Prediction of the inner potential core length for coaxial jet

The formulation adopted here is similar to the one presented in Rehab et al. (1997). The idea is that the entrained fluid has to cross the interface of where the entrainment takes place. The fluid is here assumed incompressible. With mass conservation considerations it can be argued that,

$$\frac{1}{4}\pi D_1^2 U_1 = \frac{1}{2}\pi D_1 \left[\left(\frac{1}{2} D_1 \right)^2 + x_{c,1}^2 \right]^{1/2} u_e, \tag{5.4}$$

where the left side of the equation represent the fluid injected through the inner nozzle and the right side represent the entrained fluid across the inner potential core cone.

When the annular gap is on the order of D_1, it is expected that the inner and outer potential core lengths are about equal. The entrainment velocity is then given as

$$u_e = C\alpha(U_2 - U_1), \tag{5.5}$$

where $C \approx 0.5$ is a constant determined from single jet mass conservation consideration and α is found by $u' = \kappa U_2 = \alpha(U_2 - U_1)$ in the inner mixing layer (Rehab et al., 1997). This gives the expression for the inner potential core length as

$$\frac{x_{c,1}}{D_1} = \frac{1}{2}\left(\frac{1}{C^2\alpha^2(r_u-1)^2} - 1\right)^{1/2}. \tag{5.6}$$

There is not found an explicit derivation of a predicted length of the outer potential core, $x_{c,2}$. As mentioned, Rehab et al. (1997) suggest that the inner and outer potential cores will have about the same length when the annular gap is on the order of the inner diameter, D_1.

Chapter 6

Computer simulations

The aim of this work is to investigate mixing in coaxial jets. Since the Pencil Code has never been used for simulations of jets before, simulations of a single round jet are performed to validate the code. The single jet configuration is easier than for coaxial jets, and there exists more experimental and DNS data for this case. This chapter presents how the simulations were performed.

6.1 Computational domain and boundary conditions

The simulations were performed in a rectangular box of lengths L_x, L_y and L_z. The streamwise direction is denoted x, while y and z are the normal and spanwise directions respectively. The grid spacing is constant in each direction.

The inlet boundary is the non-reflecting Navier Stokes characteristic boundary condition (NSCBC) inlet of Lodato et al. (2008). A given velocity profile is imposed for each time step at the inlet. The outlet boundary is the partially reflecting NSCBC of Poinsot and Lele (1992).

In the spanwise and normal directions, periodic boundary conditions are used. Ideally outflow boundaries should have been used at these boundaries too, but the implementation of this gave some discontinuity problems especially at the corners of the domain. It was therefore decided to use periodic boundaries to get the code to work properly and to be able to produce results.

6.2 Physical properties

The fluid in the simulations is compressible with a mean density of $\rho = 1.0$ kg/m^3. An isothermal equation of state was assumed, i.e. $P = \rho c^2$, where P is the pressure

and c is the speed of sound. The speed of sound was set to $c = 40$ m/s. A higher speed of sound requires smaller time steps, while undesirable effects start to occur if the speed of sound is too low. The speed of sound used was found sufficiently high to avoid those effects.

6.3 Velocity inlet

The shape of the velocity inlet profile prescribed for each time step is

$$\mathbf{U}(\mathbf{x}_0, t) = \mathbf{U}_{med}(\mathbf{x}_0) + \mathbf{U}_{noise}(\mathbf{x}_0, t) \cdot \mathbf{U}_{profile}(\mathbf{x}_0), \tag{6.1}$$

where $\mathbf{U}_{med}$ is the mean velocity profile, and $\mathbf{U}_{noise}(\mathbf{x}_0, t) \cdot \mathbf{U}_{profile}(\mathbf{x}_0)$ is some noise designed to get a disturbance mainly in the shear layers. The noise on the inlet is explained more in details in section 6.3.3.

6.3.1 Single jet

The mean velocity profile of the single jet is represented as

$$U_{med}(\mathbf{x}_0, r) = \frac{U_J + U_a}{2} - \frac{U_J - U_a}{2} \tanh\left(\frac{r - R}{2\theta}\right), \tag{6.2}$$

where U_J is the centerline velocity of the jet, U_a is the velocity of the coflow, R is the radius of the jet, and θ is the momentum thickness. Figure 6.1 shows a sketch of the inlet velocity profile.

The hyperbolic-tangent velocity profile is found to model the round jet flow in the near field region very well and is widely used (Michalke and Hermann, 1982). The momentum thickness is a measure of the thickness of the shear layer. It was found appropriate to use $\theta = R/13$ as in Silva et al. (2003).

6.3.2 Coaxial jet

For the coaxial jets, the shape of the mean velocity profile is

$$U_{med}(\mathbf{x}_0, r) = \begin{cases} \frac{U_1+U_2}{2} - \frac{U_1-U_2}{2} \tanh\left(\frac{r-R_1}{2\theta}\right) & \text{for } r < R_m \\ \frac{U_2+U_a}{2} - \frac{U_2-U_a}{2} \tanh\left(\frac{r-R_2}{2\theta}\right) & \text{for } r > R_m, \end{cases} \tag{6.3}$$

where $R_m = (R_1 + R_2)/2$, $\theta = R_1/2$. R_1 and R_2 is the radius of the inner and outer jets respectively. Figure 6.2 shows a sketch of the mean inlet velocity, U_1 is the inner jet velocity, U_2 is the outer jet velocity, and U_a is the coflow velocity.

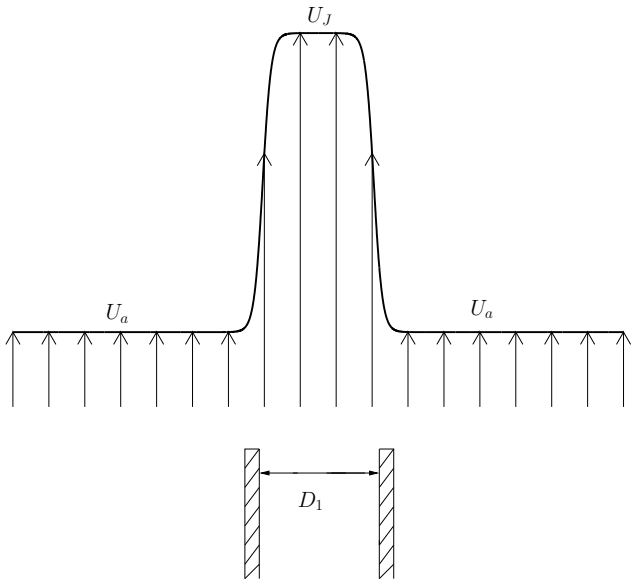

Figure 6.1: Sketch of the inlet velocity profile for the single jets. U_J is the jet velocity, U_a is the velocity of the coflow, and D is the diameter of the jet.

6.3.3 Inlet velocity perturbation

To trigger the formation of turbulent structures in the mixing layer, some noise was imposed on the inlet together with the mean velocity profile. This was done by making isotropic and homogeneous turbulence in a cube of the same size L_y and L_z as in the main rectangular box. The isotropic and homogeneous turbulence in the pre-produced turbulence-box where made by applying a large scale forced input of energy. Then the simulation was carried out until the input energy equaled the energy lost due to viscous and internal forces and a statistically steady state were obtained.

The velocity field obtained in this turbulence-box was then multiplied with a given profile to get the noise only where wanted. By looping over the normal grid planes in the turbulence-box, a new inlet condition occurred for every timestep. The next normal plane used was given by

$$\Delta x = \frac{\bar{U}}{\Delta t}, \tag{6.4}$$

where $\bar{U}$ is a mean velocity at the inlet and Δt is the timestep in the main simulation. For the single jet U_J was used as this mean velocity, while U_2 was used for the coaxial jet. Interpolation is used to find the correct normal plane to match the main simulation. The new inlet condition was then different from, but not independent of the inlet conditions in the previous timestep. When the end of the

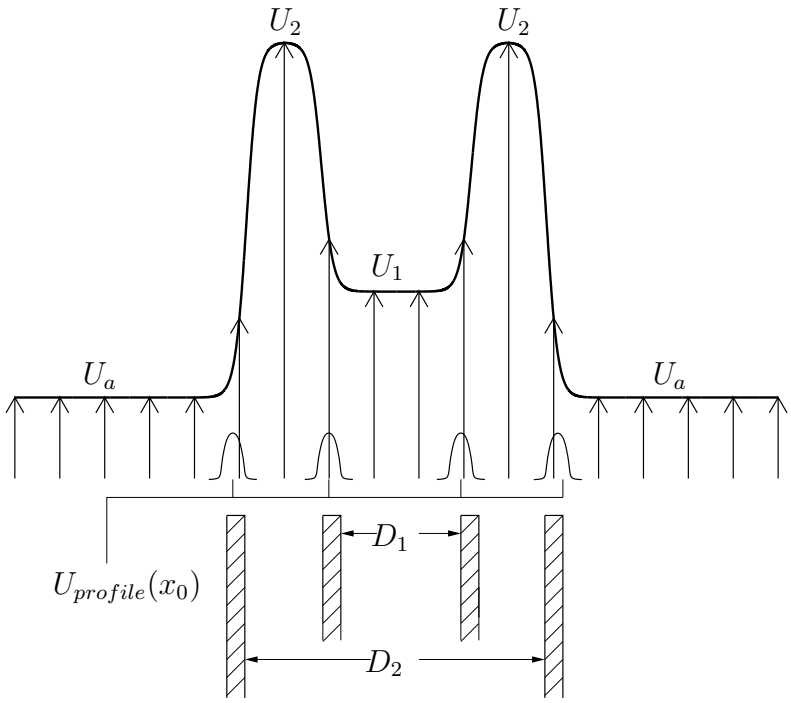

Figure 6.2: Sketch of the inlet velocity profile for the coaxial jet. U_1 is the inner jet velocity, U_2 is the outer jet velocity, and U_3 is the velocity of the coflow. The small profiles denoted $U_{profile}(x_0)$ is the region where velocity perturbation is prescribed.

turbulence-box was reached, the looping started from the beginning again.

The shape of the noise profile for the single jet was set to

$$U_{profile}(\mathbf{x}_0, r) = 0.2 \left[\frac{U_J}{2} - \frac{U_J}{2} \tanh\left(\frac{r - R_{profile}}{2\theta} \right) \right], \tag{6.5}$$

where U_J and θ are the same as in equation 6.2, and $R_{profile}$ is slightly larger than the radius of the jet. The maximum noise was 25% of U_J.

When the simulations of the single jets were analyzed, it was found that the influence from the inlet seemed to dominate the flow more than wanted. For this reason, the shape of the noise profile for the coaxial jets were made in a different manner than for the single jets. For the coaxial jets, the profile was only set in a very narrow region around the shear layers. The shape of $\mathbf{U}_{profile}(\mathbf{x}_0)$ for the coaxial jets is shown in figure 6.2. The maximum noise was about 25% of U_2 also for the coaxial jets.

6.4 The passive scalar

Turbulent mixing processes in the jets was investigated by introducing a passive scalar in the computational simulations. The transport equation for the passive scalar, C , is given as,

$$\rho\frac{\partial C}{\partial t} + \rho\mathbf{U}\cdot\nabla C = \mathcal{D}\left[\rho\nabla^2 C + \nabla\rho\nabla C\right], \tag{6.6}$$

where $\mathcal{D}$ is diffusion constant of the passive scalar. The diffusion is assumed constant (Pencil Code Manual), and its value was set to 1×10^{-4} in all simulations. The scalar is conserved and it does not affect the velocity field in any manner.

For the single jet, the passive scalar has the value one inside the jet, and zero elsewhere. For the coaxial jet, the passive scalar is given the value one inside the co-annular jet, and zero elsewhere. The passive scalar can be considered as a measure of concentration, and is sometimes also referred to as the mixing fraction.

As for the velocity, it is expected to find self-similarity for the radial concentration. The similarity coordinate used for the concentration in this work is b_{gc}, defined by the radial location at which $\langle C(x, b_{gc})\rangle = e^{-1}C_0(x)$.

Chapter 7

Results

In this chapter, the results of the direct numerical simulations are presented. Five simulations denoted RUN1-RUN5 have been performed. Table 7.1 and 7.2 show the parameters of the different simulations. Note that the domain size is given in unit of the jet's diameter.

Table 7.1: Single jet simulations

	RUN1	RUN2
Grid	1024x256x256	1024x512x512
Domain size [D]	28.6x7.1x7.1	28.6x14.2x14.2
ν [m^2/s]	6.0×10^{-5}	9.0×10^{-5}
Re= $U_J D/\nu$	1820	1213
U_J [m/s]	6	6
U_a [m/s]	0.9	0.3
Statistics time [s]	0.31	0.41
D [mm]	18.2	18.2

The 'statistics time' in the tables is the time over which the statistics were calculated. The velocity field and the concentration were saved every $\Delta t = 0.01$ s. The total CPU hours that were required to perform all the simulations was approximately 150,000, producing more than 1.5 Terra bytes of data. Interactive Data Language (IDL) and Visualization and Analysis Platform for Ocean, Atmosphere, and Solar Researchers (VAPOR) were used to visualize the results and to produce the figures in this chapter.

Table 7.2: Coaxial jet simulations

	RUN3	RUN4	RUN5
Grid	768x256x256	768x256x256	768x256x256
Domain size $[D_1]$	42.9x14.3x14.3	42.9x14.3x14.3	42.9x14.3x14.3
ν [m^2/s]	1.0×10^{-4}	1.0×10^{-4}	1.0×10^{-4}
Re$= U_2 D_1/\nu$	364	546	728
U_2 [m/s]	4	6	8
$r_u = U_2/U_1$	2	3	4
$\beta = D_2/D_1$	2	2	2
Statistics time [s]	0.94	0.62	0.73
D_1 [mm]	9.1	9.1	9.1

7.1 Single jet statistics

The first simulation, RUN1, served as a test simulation to see that the jet behaved as it should. There was no passive scalar implemented in this simulation. Figure 7.1 shows the mean values of the centerline velocity and the axial velocity at several downstream locations. As discussed in chapter 4, it was expected to find that

$$\frac{U_0(x)}{U_J} \sim \frac{1}{x - X_0} \tag{7.1}$$

$$\frac{\langle U \rangle - U_a}{U_0 - U_a} = \exp\left(-\frac{r^2}{b_g^2}\right), \tag{7.2}$$

after the potential core. Equation 7.2 is modified for jet with coflow. Figure 7.1 shows that the centerline velocity is acting more or less as it should in the first part of the domain, but that the centerline velocity decay slower than expected towards the end. In addition it is observed that the centerline velocity suddenly increases at the very end of the domain. The profile of the axial velocity is not as it should be. Instead of converging into the self-similar Gaussian profile, the profile becomes narrower and narrower downstream. It was suggested that the reason for these problems is that the domain was to small. The jet does not act right since there are periodic boundary conditions in the spanwise and normal directions. As the jet reaches the boundary, it will start to push itself together through the boundaries of the domain. The outgoing velocity field at one boundary will be the incoming velocity at the opposite boundary. This will enforce the jet to become more narrow than it would if it was evolving naturally, which again detains the centerline velocity to decay as it should.

In the second simulation of the single jet, RUN2, it was therefore decided to increase the domain size to the double in both the spanwise and the normal

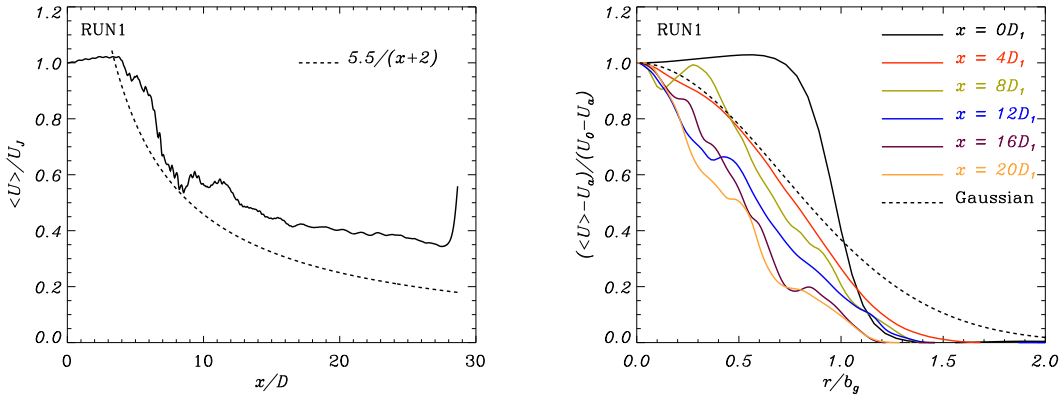

Figure 7.1: Mean centerline velocity scaled by the jet exit velocity and mean axial velocity profiles at several downstream locations. The dashed line in the right panel represent the curve fit for RUN2.

directions. In this simulation the passive scalar was also tested. This simulation was very time consuming because of the large domain, and more than 60,000 CPU hours was used for this simulation alone.

Figure 7.2 shows the same results as was shown for RUN1, the mean values of the centerline velocity and the axial velocity at several downstream locations. These results were found much more satisfying. The centerline velocity still has the sudden increase at the end of the domain. This implies that this problem is due to the outflow boundary condition rather than the domain size. Because of the influence of the outflow boundary, the statistics of the last 10 diameters of the domain are not considered. The centerline velocity is compared to experimental data from Hussein et al. (1994) and Panchpakesan and Lumley (1993). These experimental papers only consider the jets in the self-similar region, from $x = 15D$. The lines are therefore dashed for smaller x. The agreement between the simulation and the experimental data is good. The same shape is obtained, but it is seen that the potential cores of the experimental data is larger than for this simulation. The numerical results of Lubbers et al. (2001) are also presented in this figure, and it is seen that the potential core in that work is found even further downstream. Possible reasons for the differences in the potential core lengths is discussed and one reason is found to be that the disturbances imposed at the inlet are too dominant.

The mean axial velocity profiles are also found to be much better compared to the Gaussian profile than what was found in RUN1. It was expected to find self-similarity from about $x = 15D$, so it is still not perfect. A possible reason for this is that the averaging is not done over a long enough period of time. As it can seen in both panels of figure 7.2, the lines are not perfectly smooth, which also is

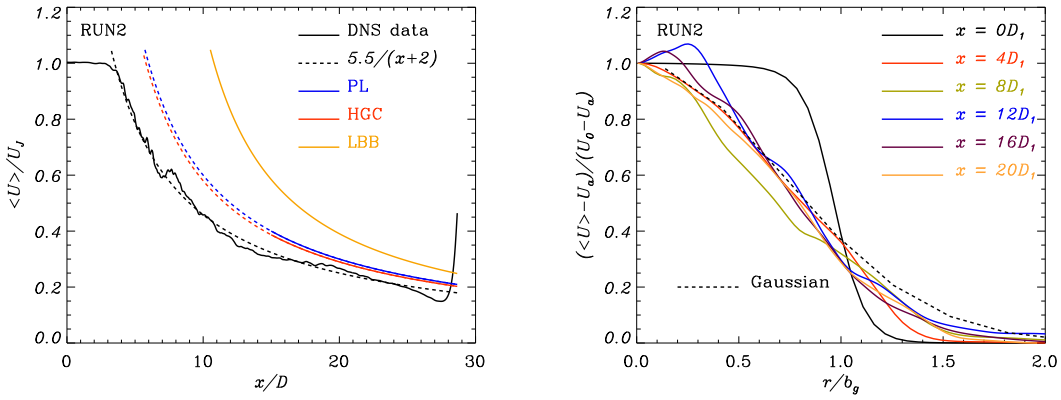

Figure 7.2: Mean centerline velocity scaled by the jet exit velocity and mean axial velocity profiles at several downstream locations. The mean centerline velocity is compared to the curve fits given in the experimental papers by Hussein et al. (1994)(HGC) and Panchpakesan and Lumley (1993)(PL) as well as in the numerical paper by Lubbers et al. (2001)(LBB).

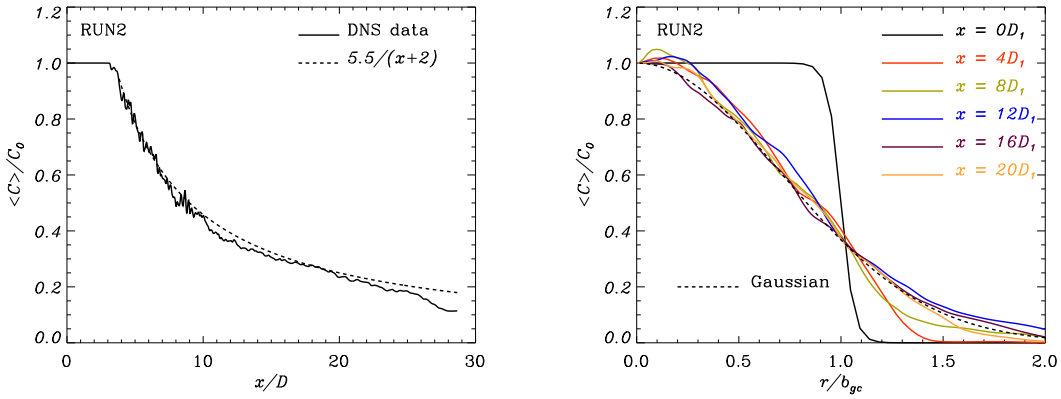

Figure 7.3: Mean centerline concentration and mean axial concentration at several downstream locations.

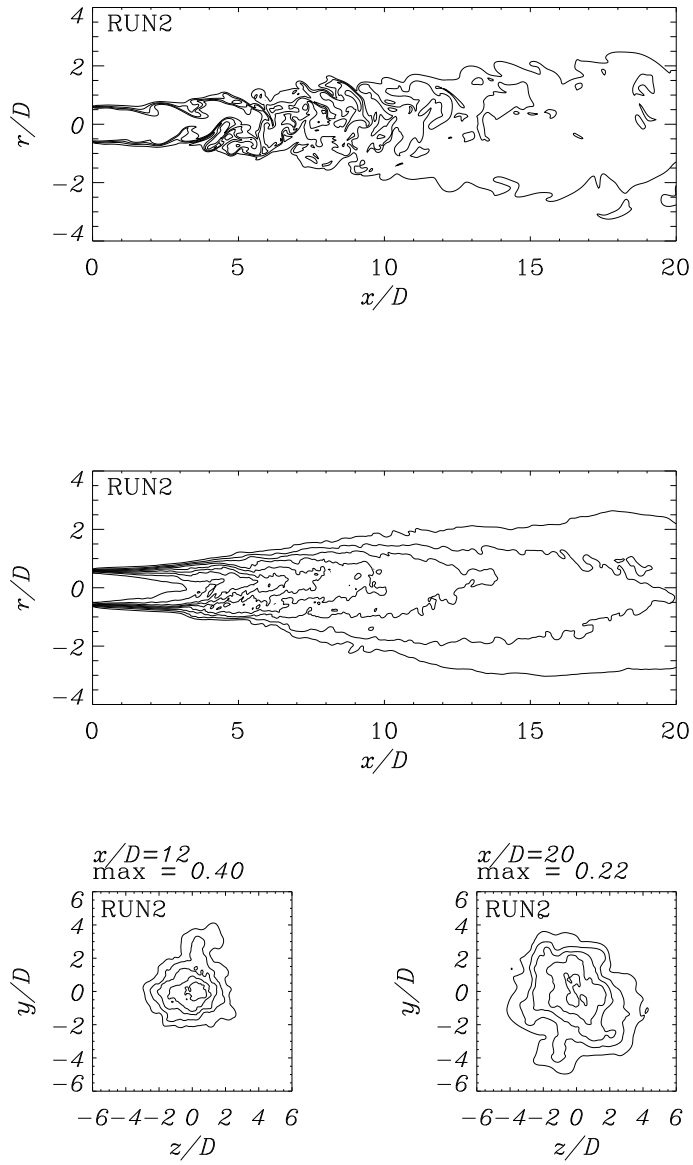

Figure 7.4: Contour plots of instantaneous and mean concentration of the jet in RUN2 with ten contour levels equally spaced from 0 to 1. The jet cross-section have 5 contour levels equally spaced. The upper panel is instantaneous, while the three others are mean values.

an indication of the same.

In figure 7.3 the mean centerline concentration and the mean axial concentration are shown. A similar behavior as the velocity field is seen. The centerline concentration starts to decay for a slightly smaller x than the velocity. The mean axial concentration profiles seem to follow the Gaussian profile better than what was found for the mean velocity. The analysis also show that generally $b_g < b_{gc}$, especially at the first 15 diameters of the domain.

Figure 7.4 shows contour plots of the concentration. The upper figure shows an instantaneous concentration distribution in the streamwise direction. The irrotational flow close to the inflow plane can be seen in this figure. Around $x = 2D$, the flow starts to roll up and becomes turbulent. In the middle panel of figure 7.4, the mean concentration is shown. Here the potential core becomes visible. The potential core is found to end at $x = 3.1D$. Both the mean concentration in the streamwise direction and the cross-section show that the jet is not completely axisymmetric. This could again imply that the averaging is not done over a long enough period. Another suggestion is that L_x in the pre-simulated turbulence-box is not long enough. In movie visualizations of the flow some periodicity can be seen. The evolution of the jet will be very dependent of the perturbations on the inlet since the simulation is performed with a relatively low Reynolds number.

All the results from RUN2 show reasonably good agreement with the DNS results of Lubbers et al. (2001). The main difference is that the potential core is shorter and the jet starts to roll up closer to the inlet in the present work. The results were considered good enough to carry on with simulations of coaxial jets. To get less influence from the turbulence on the inlet, the profiles of the forced turbulence were made smaller and only around the shear layers for the coaxial jets

7.2 Coaxial jet statistics

Due to the influence of the periodic boundaries and the outflow boundary condition on the outlet, only the first $20D_1$ of the domain is considered for the coaxial jets. Figures 7.5 through 7.7 show the statistics of the three coaxial jet simulations. In figure 7.5 the mean axial velocity profiles and the root-mean-square at several downstream locations are shown. The shape of the axial velocity profile at $x = 0D_1$ equals the imposed velocity field. At $x = 8D_1$ the profiles still have a coaxial shape, while at $x = 12D_1$ the maximum velocity is found at the centerline for all three simulations. Somewhere between this two locations, the jet loose their two-layer structures and get the shape of a single jet. The root-mean-square velocity profiles serve to represent the turbulent intensity. The most intense turbulent activity is found in the inner shear layer until $x = 4D_1$. Downstream of this the most intense turbulence is found in the outer shear layer. The magnitude and shape of the

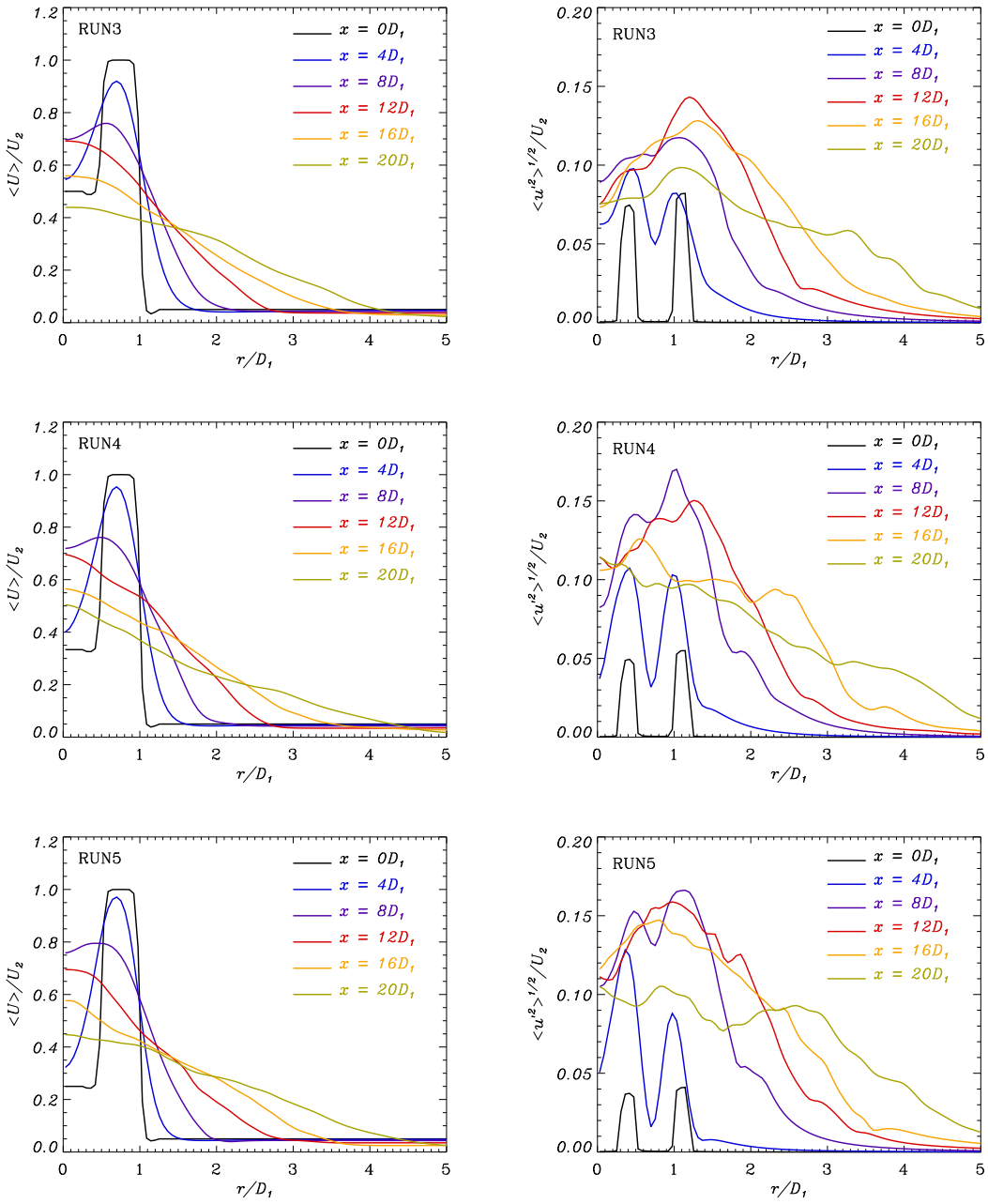

Figure 7.5: Radial evolution of the streamwise velocity and the rms velocity fluctuations at several downstream locations for the simulations of coaxial jets.

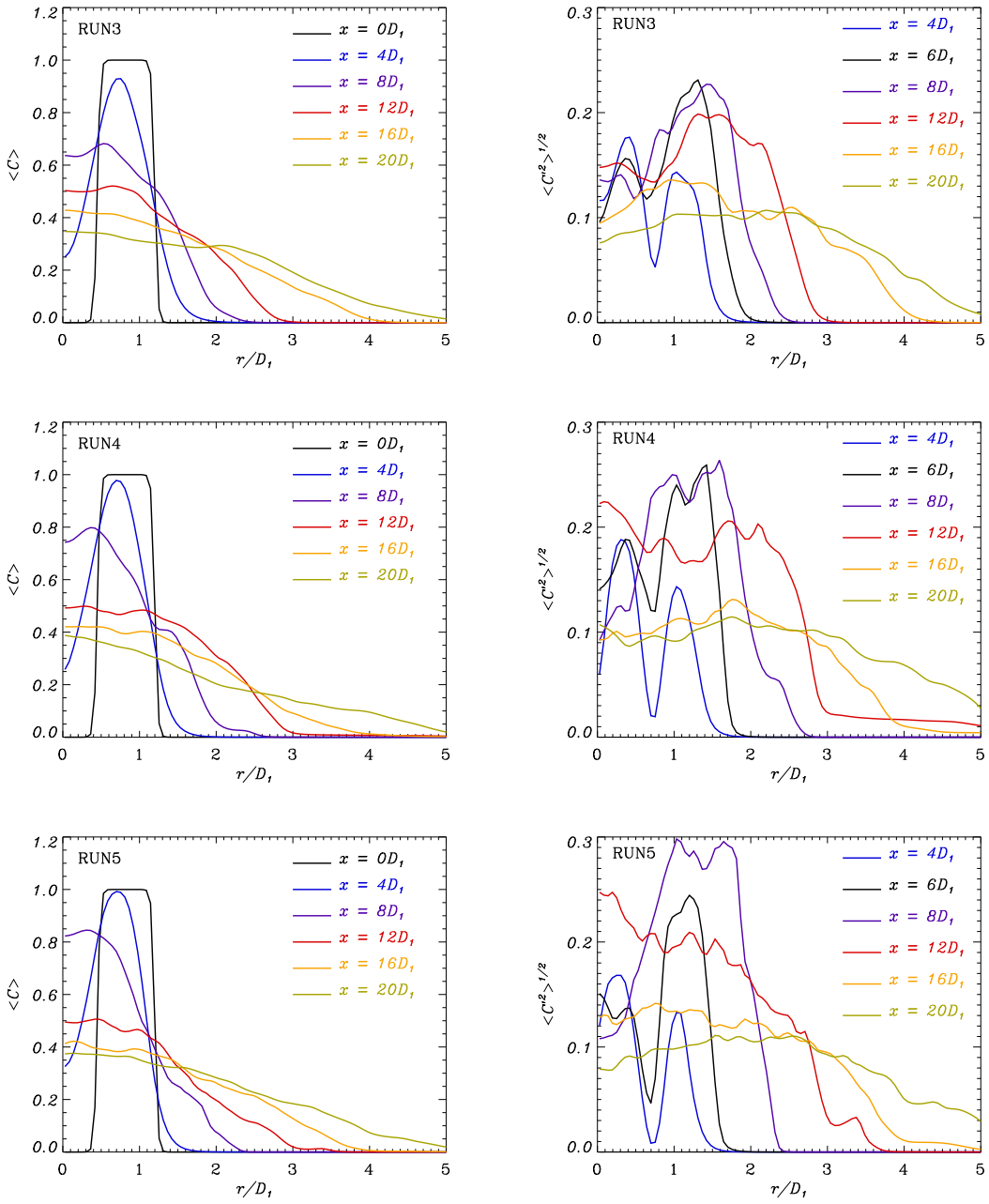

Figure 7.6: Radial evolution of the concentration and the rms concentration at several downstream locations for the simulations of coaxial jets.

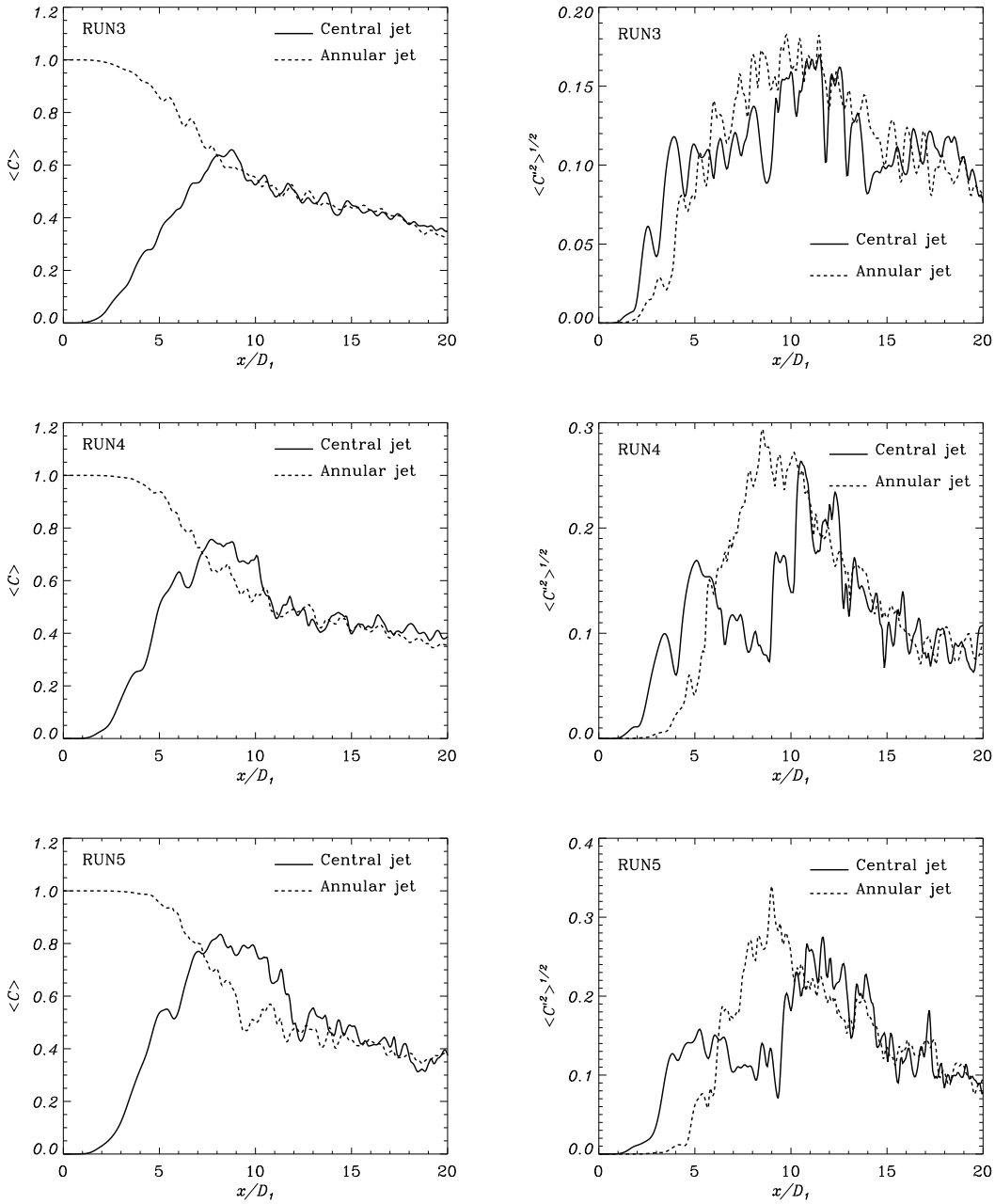

Figure 7.7: Downstream evolution of the concentration and downstream evolution of the rms concentration in both central and annular jet for the simulations of coaxial jets. The central jet line corresponds to the centerline, while the annular jet line is in the middle of the the outer jet at the inlet.

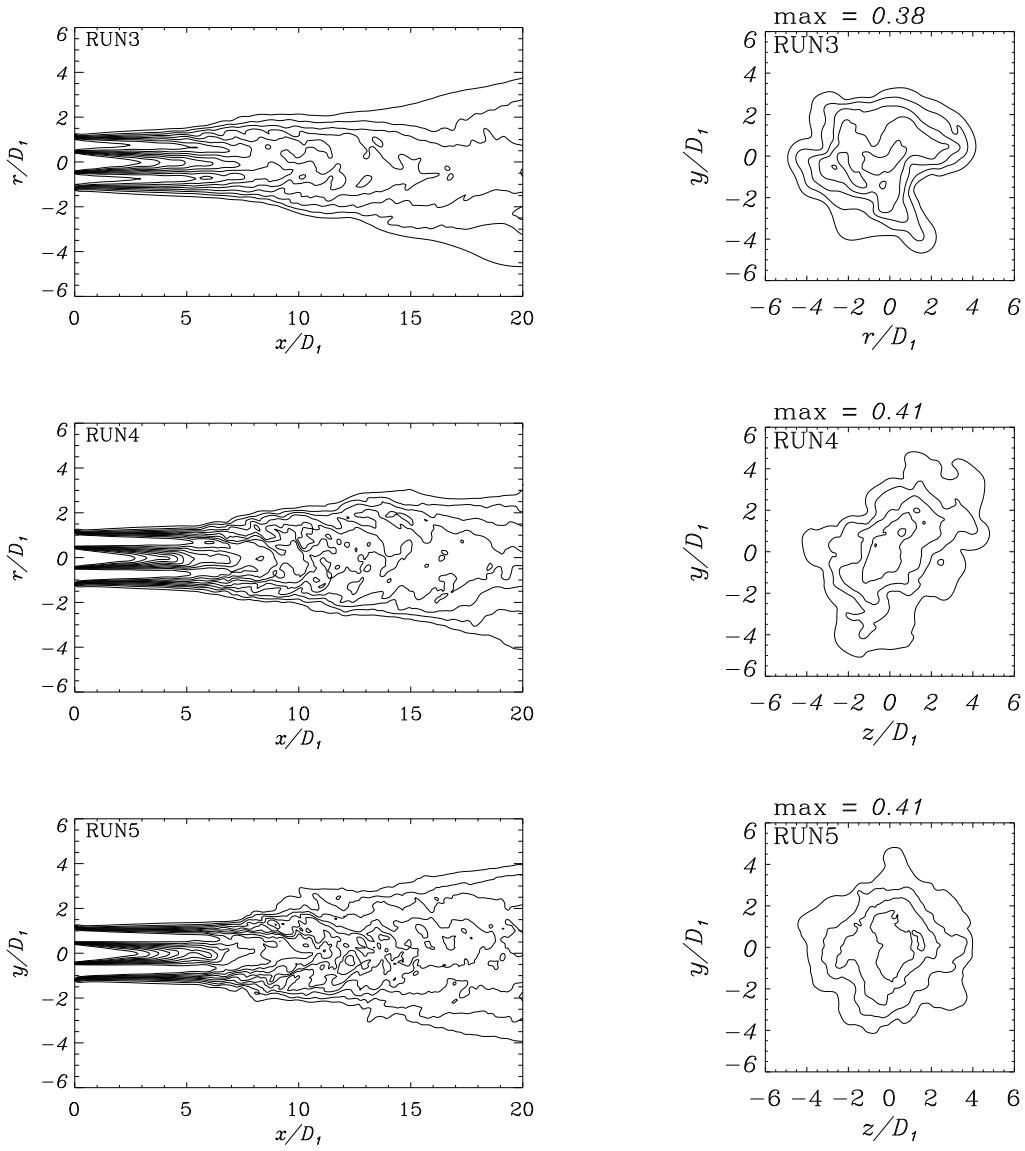

Figure 7.8: Contour plot of the mean concentration of the jet with ten contour levels equally spaced from 0 to 1. The jet cross-section have 5 contour levels equally spaced.

intensities are in good agreement with the result of Balarac and Si-Ameur (2005) where a coaxial jet with $r_u = 5$ were simulated. They found a maximum turbulent intensity at $x = 10D_1$ with the magnitude $0.18U_2$. The experimental investigations of Warda et al. (1999) on the other hand found a maximum turbulent intensity at $x = 14D_1$ with the magnitude of $0.11U_2$, when $r_u = 1.6$

The radial evolution of the concentration and the root-mean-square concentration at several downstream location are shown in figure 7.6. The concentration plots show a similar tendency as the velocity plots. It can also be seen that the concentrations profiles are wider than the velocity profiles. This is the same that was found for the single jet in RUN2, and is in good agreement with the preferential transport of the scalar over the momentum (Pope, 2000).

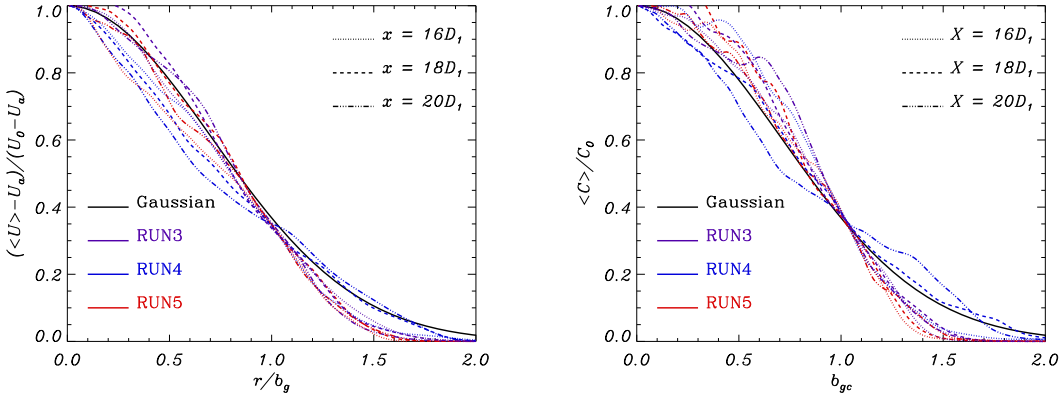

Figure 7.9: Radial evolution of the velocity and the concentration at the last downstream locations in the domain scaled by the similarity coordinate b_g and b_{gc} respectively for the simulations of coaxial jets.

Figure 7.7 shows the streamwise evolution of the concentrations and the root-mean-square values of the concentration. The figures for the concentrations show that for larger r_u, larger values of concentration at the centerline are obtained. The values of the concentration fluctuations are also larger for larger velocity ratios. Compared to Balarac and Si-Ameur (2005) it is seen that the centerline concentrations starts to increase closer to the inlet than what they found. The same apply for the concentration in the annular jet, it starts to decrease closer to the inlet. Except for this, all the figures 7.5 through 7.7 show good agreement to Balarac and Si-Ameur (2005).

Contour plots of the mean concentrations are given in figure 7.8. As for the single jet, it is again seen that the jets are not perfectly axisymmetric. Together with the fact that the curves in the figures 7.5 through 7.7 are not very smooth, this suggests that the averaging is not done over a long enough period of time. Due to

the fact that the simulations were very time consuming and the time limitations in this work, there was not enough time to run the simulations further. The potential cores are clearly visible in the figure.

In figure 7.9 the radial velocity and the concentration scaled by the similarity coordinates is shown for some of the last downstream locations in the flow. It can be seen that the coaxial jets show a good tendency of self-similarity at these locations. Especially the figure of the centerline velocity shows promising results. The results for the concentrations are not as smooth as for the velocities. It is also seen that specially the results from RUN4 deviate from the Gaussian shape. RUN4 is averaged over less amount of time than the two others, which may be the cause of this discrepancy.

7.3 Prediction of potential core lengths

Table 7.3 gives the x-coordinate at the end of the potential cores. The theoretical values derived from equations 5.3 and 5.6 are also shown..

Table 7.3: Potential core lengths in units of D and D_1

	RUN2	RUN3	RUN4	RUN5
$x_{c,1}$	3.3	1.4	1.4	1.4
$x_{c,2}$	-	2.0	3.9	4.7
$x_{c,1}$,theory	7.0	8.3	6.7	6.3

Remembering that $u' = \kappa U_2 = \alpha(U_2 - U_1)$ in equation 5.6 it was found that,

$$u' \simeq \begin{cases} 0.06U_2 = 0.120(U_2 - U_1) & \text{for } r_u = 2 \text{ (RUN3)} \\ 0.05U_2 = 0.075(U_2 - U_1) & \text{for } r_u = 3 \text{ (RUN4)} \\ 0.04U_2 = 0.053(U_2 - U_1) & \text{for } r_u = 4 \text{ (RUN5).} \end{cases} \tag{7.3}$$

The actual lengths of the potential cores found by analyzing the simulated jets are not in agreement with the predicted ones. As mentioned, it was found that the single jet starts to roll-up closer to the inlet for the present work than what it does in the simulation performed by Lubbers et al. (2001) . The same was the case for the coaxial jets compared to the simulation performed by Balarac and Si-Ameur (2005).

Again, the influence of the pre-simulated turbulence-box has to be considered as a possible reason for the deviation. Since the amplitude of the inflicted noise

is about 25% of the jet velocities, it seems to affect the jets evolution more than what would be the case for a natural evolving jet.

Another observation is that for the coaxial jets, the outer potential cores are longer than the inner ones. The equation 5.6 were derived assuming that the inner and outer cores were approximately the same length. Most likely, the equation can not be used when the outer potential core is longer than the inner. The flow in the inner jet gets trapped between the outer cores in a very different way than when the outer potential core is shorter than the inner one.

In the simulations of the coaxial jets in this work, $\beta = 2$ was used. This is the same as was used in Silva et al. (2003). They found that both the inner and outer potential cores ended at $x = 5D_1$ when they used $r_u = 3.3$. Except from Silva et al. (2003) most publications on coaxial jets make use of a smaller outer to inner diameter ratio. Even though it is emphasized in Rehab et al. (1997) that the prediction of potential core is valid for large annular gaps, it is not not certain that it applies to such big annular gap as used in this work. The simulations in this work keep the inner jet exit velocity constant, while the outer jet exit velocities are varied. This differs from the most published work on coaxial jets, which rather keep the outer jet velocity constant in their investigations.

7.4 Visualization of the coaxial jets

Figure 7.10 shows three dimensional visualizations of the coaxial jet simulations to $x = 20D_1$. The visualization gives a good picture of the flows. The colored figures show the instantaneous concentrations of the passive scalar. It can be seen that for the larger velocity ratios the jets keep their initial shape for a longer distance. In addition it is seen that smaller structures are visible for higher r_u. This is reasonable since higher Reynolds number gives smaller scales.

The right panel of figure 7.10 shows iso-surfaces of positive Q. Q is the second invariant of the velocity gradient tensor,

$$Q = \frac{1}{2}\left(\Omega_{ij}\Omega_{ij} - S_{ij}S_{ij}\right), \tag{7.4}$$

where $S_{ij} = \frac{1}{2}(\frac{\partial u_i}{\partial x_j} + \frac{\partial u_j}{\partial x_i})$ is the rate of strain tensor and $\Omega_{ij} = \frac{1}{2}(\frac{\partial u_i}{\partial x_j} - \frac{\partial u_j}{\partial x_i})$ is the vorticity tensor. Note that S_{ij} not is the traceless rate of strain tensor used in equation 2.1. Q is a good indicator of coherent vorticities, as it defines regions of both high local vorticity and low rate of deformations (Neto, 2008).

In the near field flow it can be seen that the structures have what can be identified as helical shaped vortex rings located in the shear layers. This is as expected according to Silva et al. (2003). Further downstream growing of smaller scale turbulence begins. Again it is seen that smaller scales are present in the higher

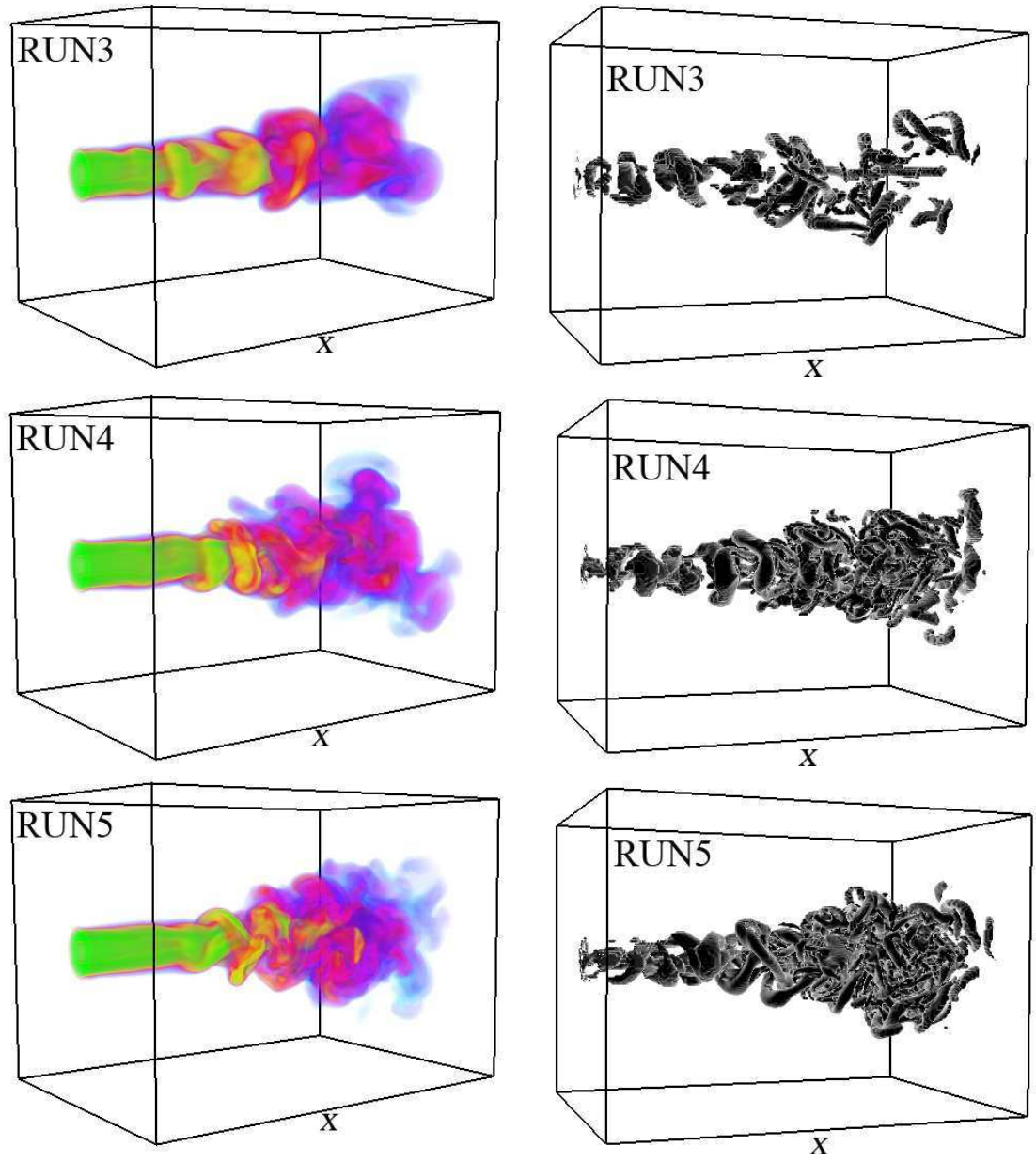

Figure 7.10: Visualizations of the coaxial jets. The figures to the left show the instantaneous concentration where green indicates high and blue indicates low concentration. The figures to the right show instantaneous iso-surfaces of positive Q.

velocity ratio simulations. As the smaller scales become apparent the structures seem to loose their preferential directions for RUN4 and RUN5. This indicates that the jets have reached a state of fully developed turbulence (Silva et al., 2003). The same effect is not visible in RUN3.

The lowest Reynolds number is found in RUN3 with Re=364. The visualization of Q makes it clear that this is to low to get a fully turbulent flow. The viscous forces in the flow destroy the eddies before they get the chance to develop fully.

7.5 Turbulent mixing in coaxial jets

As the main scope of this study was to investigate mixing in coaxial jets, the properties of the mixing are summed up in this section.

The three simulations RUN3 through RUN5 showed relatively similar spatial evolution. The figures 7.5 and 7.6 show that the coaxial jets have lost their two-layer structures at $x \approx 12D_1$. With more careful investigation it was found that for RUN3 this happens at $x \approx 11$ and at $x \approx 9$ for RUN4 and RUN5. The three-dimensional visualizations of the jets made it clear that RUN3 had not reached fully developed turbulence. It is therefore not considered in the further investigations.

As seen in figure 7.7, the concentration in the inner jet reaches the same value as in the outer jet at $x \approx 7D_1$ for both RUN4 and RUN5. At this location, the mixing fraction is 0.7 for RUN4 and 0.8 for RUN5. Then the mixing fraction increases further in the inner jet and gets a maximal value of 0.75 for RUN4 and 0.85 for RUN5, before it again gets the same value as in the outer annular jet. This happens at $x \approx 11D_1$ and $x \approx 12D_1$ for RUN4 and RUN5, respectively. At these locations the mixing fraction is 0.5 for both simulations. Beyond this point both the mean concentrations and the root-mean-square concentrations have more or less the same values. Figure 7.9 showed that even further downstream at $x = 16D_1$ the concentration profiles became approximately self-similar.

In the present work it was found that the inner potential cores had the same length, whereas the outer potential length increased with increasing velocity ratios. Taking into account that the simulations were done with a very low Reynolds number, it is assumed that the inlet perturbations give a big contribution to how the jets evolve in the near field. All the simulations of the coaxial jet used the same turbulence-box for the inlet velocity perturbations, though it is hard to know how much this affected the evolving of the jets in the near field. Another important aspect is that in the present work the coaxial jets with higher velocity ratios also have a larger Reynolds number. This makes it hard to know what is an effect of larger Reynolds numbers and what is an effect of the differences in the velocity ratios.

It is hard to make general conclusions about mixing in coaxial jets from these

observations. In these particular cases it is seen that at about $4D_1$ to $5D_1$ downstream of the end of the potential cores, the coaxial jets get the shape of a single jet. Further downstream the jets also obtain self-similarity, and it can be assumed that mixing properties of single jets will apply in this region. If the theory behind the predictions of potential core lengths was studied closer, and a more general expression was found, it would likely be possible to predict when the coaxial jets start to act like a single jet. This theory should probably take the Reynolds number, the outer to inner diameter ratio and the velocity ratio into account. It would also be important to study the influence from the imposed perturbation in the inlet velocity closer.

Chapter 8

Discussion

In this chapter some of the issues concerning the simulations and the results are discussed. Some of the possible sources of error have already been mentioned. An attempt to sum up all of the possible errors is done here.

8.1 Inlet velocity perturbation

First the possible influence of the periodicity due to the pre-simulated turbulence is investigated closer. Figure 8.1 shows the minimum streamwise velocity in the domain as a function of time. From this figure it becomes clear that there is a periodicity in the flow. The period for this periodicity is about 0.06 s, which is the same as the time used for looping over the normal grid planes in the turbulence-box.

The amplitude of the maximal noise on the shear layers was most likely much higher than what was necessary to trigger the formation of turbulent structures. In addition to the statistics not being averaged over a long enough period of time due to time limitations in this work, this could also be a reason for perfect axisymmetry not being obtained.

8.2 Boundary conditions

Periodic boundaries in the spanwise and normal directions were briefly discussed earlier in chapter 7. When the boundary of the jet start to approach the edges of the domain in the spanwise and normal directions, it will push the jet together through the periodic boundaries. To avoid the influence of this problem, the domain was made relatively large. Only the first part of the domain was considered when the results were analyzed. This was also done to avoid possible influence from the outlet, which also behaved unexpectedly.

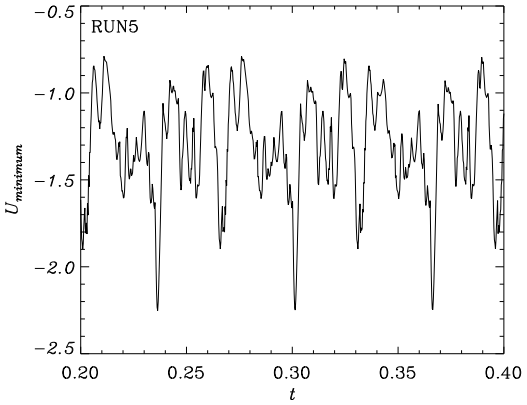

Figure 8.1: Minimum streamwise velocity in the domain as a function of time. Periodicity due to the pre-simulated turbulence is observed

To get better results it would be important to find a good solution for the outlet boundary conditions at the spanwise and normal boundaries, as well as to find a better solution at the streamwise outlet. This would make it possible to use a smaller domain and the simulations would be less time consuming, making it possible to do simulations with higher Reynolds number.

8.3 Momentum conservation

Another worrying problem found when analyzing the simulations is due to conservation of momentum. It was found that the total streamwise momentum flux decreases significantly downstream in the simulations. Figure 8.2 shows the downstream evolution of the total streamwise momentum in the domain. It is observed that the total momentum differs by about 1% for RUN2 and 5.5% for RUN5. The Pencil Code solves the equations of motion in a non-conservative form. Thus, the conserved quantities will only be conserved up to the discretization error of the scheme (Pencil Code Manual).

The decrease in the momentum flux is then an indication of the Reynolds numbers being too high. During movie visualizations of the single jet test simulations "wiggles" in the vorticity field were observed. According to the Pencil Code manual, the presence of "wiggles" indicates that the simulation is under-resolved. To avoid this, the simulated fluid was made more viscous for the coaxial jets. This resulted in relatively low Reynolds numbers. However, "wiggles" were still found in the coaxial jet simulations. The consequences of the discretization error are not

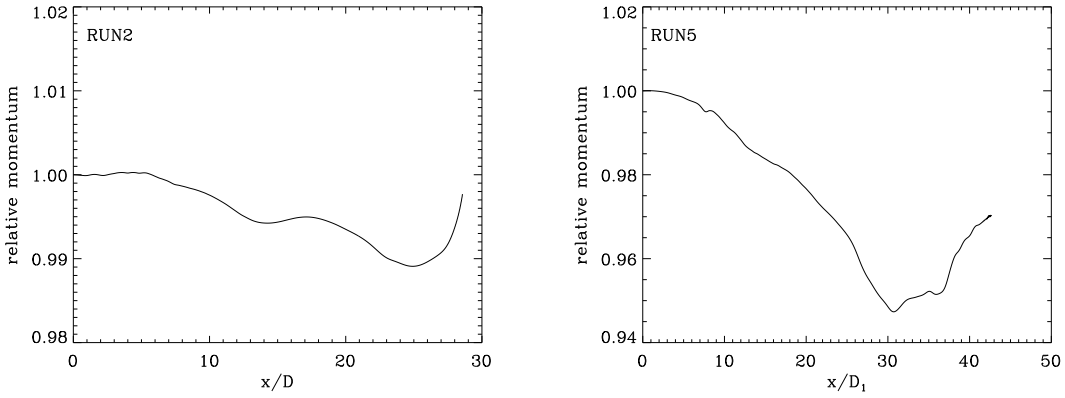

Figure 8.2: Relative downstream momentum flux. A significant momentum loss is observed.

known.

8.4 The Reynolds number

Table 7.2 shows that the Reynolds number differs in the three simulations of coaxial jets. The coaxial jet with highest velocity ratio also have the largest Reynolds number. When analyzing the results, this makes it hard to know what is an effect of the Reynolds number and what is an effect of the different velocity ratios. A different approach would be to change just one of the parameters at a time.

Another concern considering the Reynolds number is that they are very low. For comparison, the lowest Reynolds number is ten times smaller in the present work than what was used in Silva et al. (2003). As discussed in chapher 2, this is a limitation with direct numerical simulations. However it was found that the Reynolds number in RUN3 was too low to get fully developed turbulence. This is also a good argument for keeping the outer jet exit velocity constant and rather vary the inner jet exit velocity.

Chapter 9

Conclusion

Mixing of a passive scalar in coaxial jets was studied numerically using direct numerical simulation. The coaxial jets had hyperbolic mean velocity profiles that were imposed at the inlet. A pre-simulated turbulence-box was used to make disturbances in the shear layers at the inlet. Three different cases with different outer to inner jet velocity, $r_u = 2$, 3 and 4, were investigated keeping the inner jet exit velocity constant. The inner to outer jet diameter ratio, $\beta = 2$, was the same for all three cases. The three simulations all showed promising results compared to existing literature. In addition to the coaxial jets, test simulations of single round jets were performed for validation of the code. The code used was the Pencil Code.

The passive scalar was set to one inside the co-annular jet and zero elsewhere. For larger r_u it was found that the maximum concentration at the centerline reached larger values. The root-mean-square fluctuations of the concentration also got larger values for larger outer to inner jet velocities ratio. Due to this observations it can be concluded that higher velocity ratio give more rapid mixing. However, it is hard to say what the effect of the velocity ratio is considering the fact that the higher velocity ratio jets have larger Reynolds number. Larger Reynolds number also results in more rapid mixing.

It was found that the coaxial jets lost their two-layer structures at a distance about $5D_1$ downstream of the end of the potential cores. Further downstream fully developed turbulence was obtained for the two jets with highest Reynolds numbers. At a distance $x \sim 16D_1$ from the inlet the coaxial jets became approximately self-similar.

The present work serves in many ways as pioneer work in adapting the Pencil Code for use on turbulent jets. When analyzing the obtained results many issues concerning the simulations were brought up. Still the results are of qualitative value. The tendencies in the results are reasonable, considering the discussed issues in the simulations. Due to the promising results, it can be concluded that the Pencil Code absolutely can be used in further investigations of turbulent jets.

Bibliography

G. Balarac and M. Si-Ameur. Mixing and coherent vortices in turbulent coaxial jets. *C. R. Mecanique*, 333:622–627, 2005.

P.C.K. Chu, J.H. Lee, and V.H. Chu. Spreading of turbulent round jet in coflow. *Journal of Hydraulic Engineering*, 125(2):193–204, 1999.

W.J.A Dahm and P.E. Dimotakis. Mixing at large Schmidt number in the self-simiar far field of turbulent jets. *Journal of Fluid Mechanics*, 217:299–330, 1990.

W.J.A. Dahm, C.E. Frieler, and G. Tryggvason. Vortex structure and dynamics in the near field of a coaxial jet. *Journal of Fluid Mechanics*, 241:371–402, 1992.

K.K.J.R. Dinesh, A.M. Savill, K.W. Jenkins, and Kirkpatrick M.P. A study of mixing and intermittency in a coaxial turbulent jet. *Fluid Dynamics Research*, 42(2), 2010.

N. Enjalbert, D. Galley, and L. Pierrot. An entrainment model for the turbulent jet in a coflow. *C. R. Mecanique*, 337, 2009.

J.H. Hussein, S.P. Capp, and W.K. George. Velocity measurements in a high-Reynolds-number momentum-conserving, axisymmetric, turbulent jet. *Journal of Fluid Mechanics*, 258:31–75, 1994.

J.H.W. Lee, V. Chu, and V.H. Chu. *Turbulent jets and plumes: a Lagrangian approach*. Kluwer Academic Publishers, 2003.

G. Lodato, P. Domingo, and L. Vervisch. Three-dimensional boundary conditions for direct and large-eddy simulation of compressible viscous flows. *Journal of Computational Physics*, 227:5105–5143, 2008.

C.L. Lubbers, G. Brethouwer, and B.J. Boersma. Simulation of the mixing of a passive scalar in a round turbulent jet. *Fluid Dynamics Research*, 28:189–208, 2001.

M. Michalke and G. Hermann. On the inviscid instability of a circular jet with external flow. *Journal of Fluid Mechanics*, 114:343–359, 1982.

MIT Open Courseware. *Basics of Turbulent Flow*, 2002. URL `http://dspace.mit.edu/bitstream/handle/1721.1/37147/1-061Fall-2002/OcwWeb/Civil-and-Environmental-Engineering/1-061Transport-Processes-in-the-EnvironmentFall2002/LectureNotes/detail/7-lec.htm`.

P. Moin and K. Mahesh. Direct numerical simulation: A tool in turbulence research. *Journal of Fluid Mechanics*, 30:539 – 578, 1998.

P.M.R.F. Neto. Numerical simulation of turbulent accelerated round jets for aeronautical apllications. Master's thesis, Technical university of Lisbon, 2008.

N.R. Panchpakesan and J.L Lumley. Turbulence measurements in axisymmetric jets of air and helium. part 1. air jet. *Journal of Fluid Mechanics*, 246:197–223, 1993.

Pencil Code Manual. *The Pencil Code: A High-Order MPI code for MHD Turbulence*, 2009. URL `http://www.nordita.org/software/pencil-code/`.

T.J. Poinsot and S.K. Lele. Boundary conditions for direct simulations of compessible viscous flows. *Journal of Computational Physics*, 101:104–129, 1992.

S.B Pope. *Turbulent Flows*. Cambridge University Press, 2000.

H. Rehab, E. Villermaux, and E.J. Hopfinger. Flow regimes of large-velocity-ratio coaxial jets. *Journal of Fluid Mechanics*, 345:357–381, 1997.

C.B. da Silva, G. Balarc, and O. Métais. Transition in high velocity ratio coaxial jets analysed from direct numerical simulations. *Journal of Turbulence*, 4, 2003.

H. Tennekes and J.L. Lumley. *A First Course in Turbulence*. The MIT Press, ninth edition, 1983.

E. Villermaux and H. Rehab. Mixing in coaxial jets. *Journal of Fluid Mechanics*, 425:161–185, 2000.

H.A. Warda, Kassab S.Z, Elshorbagy K.A., and E.A. Elsaadawy. An experimental investiagtion of the near-field region of a free turbulent coaxial jet using LDA. *Flow measurement and Instrumentaion*, 10:15–26, 1999.

F.M. White. *Fluid Mechanics*. McGraw-Hill, fifth edition, 2005.